Effect of hot rolling parameters on recovery mechanism in 436 (17%Cr, Nb-Mo) ferritic stainless steel

M Salojee[1,a], KA Annan[1,b], CW Siyasiya[1,c], J Moema[2,d]

[1] *University of Pretoria, Department of Materials Science and Metallurgical Engineering, Private bag X20, Hatfield 0002, Pretoria, South Africa*
[2] *Advanced Materials Division (AMD), Mintek, 200 Malibongwe Drive, Randburg, 2125, South Africa*
Email: [a] *u13271050@tuks.co.za,* [b] *kofi.annan@up.ac.za,* [c] *charles.siyasiya@up.ac.za,* [d] *josephm@mintek.co.za*

Abstract

Ferritic stainless steel (FSS) grades are widely used for applications that require high strength and corrosion resistance. Their cost and versatility in the steel market have attracted a lot of interest from both industry and academic research. Despite their desirable properties, these steels grades experience surface defects as a result of microstructural evolution that evolves due to softening mechanism. The current study simulated the roughing hot rolling processes of AISI 436 (17%Cr, Nb-Mo) FSS to study the effects of inter-pass time and strain on the precipitation behaviour and the softening mechanisms in 436 FSS. The softening mechanisms and the resulting microstructures were investigated using SEM-EBSD technique. The results revealed Particle Stimulated Nucleation of new grains during the simulated roughing rolling which promoted recrystallisation due to strain accumulation. Stored deformation energy was found to increase with an increase in interpass time and strain.

Keywords: Ferritic Stainless Steel (EBSD), Hot Rolling, Dynamic Recrystallisation (DRX), Microstructure

1. Introduction

The 436 FSS is niobium stabilised with further addition of molybdenum to improve corrosion resistance. It is used in a wide range of applications from motor car exhaust trimmings to household appliances such as utensils due to their high strength and corrosion resistance (Uananisa, et al., 2016; Columbus Stainless Steel Pty Ltd, 2020; Damstahl, 2015). Studies have shown that surface ridging manifests due to inconsistent grain distributions inherited from casting and hot rolling resulting in anisotropic plastic deformation properties (Maa, et al., 2019; Annan, 2012; Maruma., 2013; Braga, 2016; Lefebvre, 2014).

The 436 Ferritic Stainless Steel does not undergo austenite to ferrite phase transformation thus limiting opportunities for grain refinement and nucleation of new phases upon cooling. The only means of grain refinement and texture randomisation may occur during recrystallisation through controlled thermomechanical processing (TMP) (Braga, et al., 2016; Mehtonen, et al., 2014). In this type of steel, shear bands are known to act as sites of nucleation for recrystallisation at grain boundaries and grain interiors (Engler & Randle, 2010; Mehtonen, 2014; Zhang, et al., 2011; Huang & Logé, 2016). The recrystallization is however reported to occur at lower deformation temperatures (Huang & Logé, 2016; Modak, et al., 2018)

The Taylor factor (TF) is a measure of the amount of slip that can occur per unit strain whereby grains with low TF are hard to recrystallize because localised deformation within the grain interior is limited. High TF grains on the other hand are known to preserve high stored deformation energy enhancing shear bands formation and subsequent recrystallisation (Zhang, et al., 2011; Mehtonen, 2014).

According to the classical theory of nucleation, both precipitation and recrystallisation prefer to nucleate on sites with higher driving force for nucleation (Siyasiya, 2007). Thus, recrystallisation cannot be studied without reference to the precipitation behaviour under such conditions. It has been reported that lower deformation temperatures provide enough driving force for precipitation of refined particles which are effective in grain boundary pinning (Siyasiya, 2007; Mandal, et al., 2018; Annan, et al., 2018). Uniform dispersed small size precipitates are effective in pinning the grain boundary migration and consequently suppresses the onset of discontinuous dynamic recrystallisation (DDRX) (Huang & Logé, 2016; Mandal, et al., 2018).

It is however worthy to note that not much attention has been given to the effect of inter-pass time and strain on the deformation behaviour of 436 FSS. The current study, therefore, focuses on the effect of inter-pass time, strain, and precipitation behaviour on the recrystallisation and the subsequent microstructural evolution in 436 FSS.

2. Experimental material and methods

The material used in the current study is industrially produced AISI 436 FSS. The as-received sample was a continuous cast slab of 190 mm thickness. At quarter thickness the slab exhibits columnar grains whilst the surfaces and the centre equiaxed grains are found. Samples were machined from the columnar area to simulate worst-case scenarios of the cast structure. Table 1 presents the chemical

Table 1: Chemical composition (wt. %) of steel used in the study

C	Mn	Si	Mo	Cr	P	S	Nb
0.12	1.00	1.00	1.00	17.00	0.04	0.03	0.70

composition of the steel used in the study and Figure 1 the as received sample.

Figure 1: As received macro etched structure of slab depicting central equiaxed grains, edge zone chill grains and quarter thickness columnar

Theoretical prediction of the precipitation behaviour and phases in the steel within the deformation conditions were studied using the TCFE6 database in the ThermoCalc software which served as a guide in choosing the deformation conditions.

The as-received cast samples were characterized to identify the columnar grain areas for the hot rolling simulations. Cylindrical samples of 10 mm diameter and 15 mm long were machined from the as-cast columnar grain structure zones. The samples were then deformed in three passes under uniaxial compression tests along the axis of the columnar grains, simulating the slab rolling. The tests were carried out using the Gleeble 1500D® thermomechanical simulator following the deformation parameters in Table 2. The control test was set to simulate roughing conditions comparable to the plant conditions. Samples were heated to 1080 °C at a rate of 20 °C /s and soaked for 300 s to achieve temperature and microstructure equalization. The strain rate was fixed at 5/s due to the Gleeble machine constraint. After the

Table 2: Experimental schedule for simulating the roughing hot rolling process

Trial	Parameter	Pass number		
		1	2	3
Control	Inter-pass time (s)	11	14	18,3
	Strain	0.18	0.24	0.3
	Temperature (°C)	1000	950	930
T1	Inter-pass time (s)	15	20	25
	Strain	0.18	0.24	0.3
	Temperature (°C)	1000	950	930
T2	Inter-pass time (s)	15	20	25
	Strain	0.24	0.3	0.3
	Temperature (°C)	1000	950	930

deformation, samples were immediately quenched to freeze the deformation structure at a rate of 600 °C/s.

Uniaxially compressed samples were sectioned parallel to the deformation axis along the sample centre and metallographically prepared for microstructure and EBSD analysis. Whilst the microscope analysis samples were grounded and polished down to 1 micron, the EBSD samples were further electro-polished using A3 solution for 20 s at 23 V and 0.2 A to remove the mechanically deformed layer. The mechanically polished samples were etched in aqua regia solution and the images observed under an Olympus BX51M microscope.

The electro-polished samples for EBSD analysis were observed in a Joel JSM 6300 scanning electron microscope using a working distance of 20 mm with an accelerating voltage of 20 kV and an inclination angle of 70°.

3.   Results and Discussions

3.1   Theoretical predictions using ThermoCalc

Figure 2 shows the ThermoCalc predicted precipitates and phases under equilibrium conditions in the hot working temperature range of 1273 and 1203 K. Three main types of precipitates are predicted
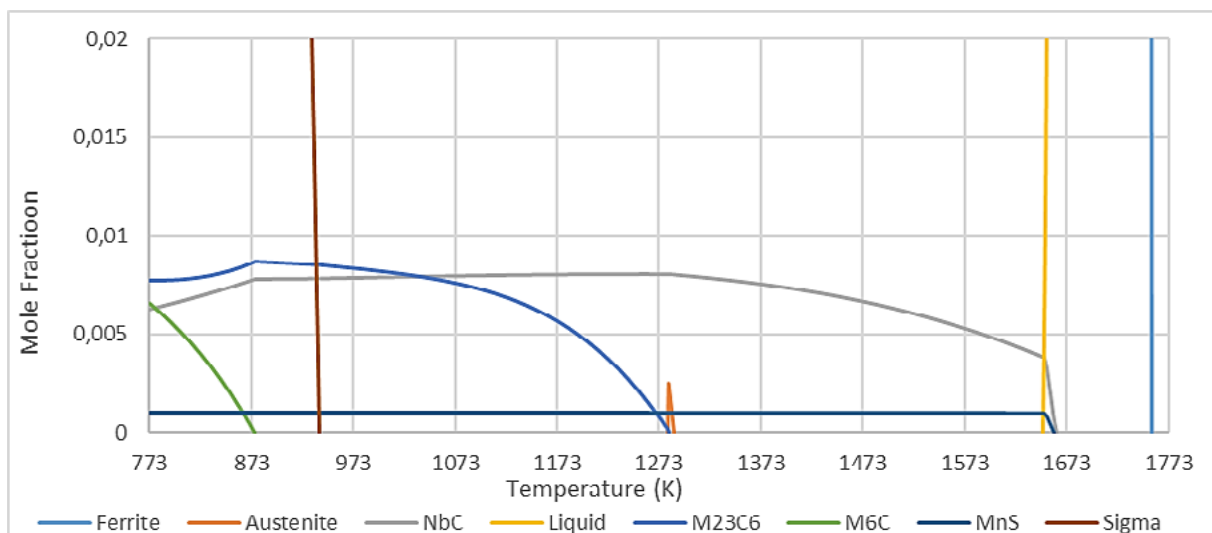
Figure 2: Prediction of volume fraction of precipitates and phases expected from 436 (Thermo-Calc Software, 2019)

namely, $M_{23}C_6$, NbC, and MnS precipitates. In other words, the precipitate that is expected to influence recovery mechanisms the most is NbC.

NbC tends to prefer nucleation at high dislocation sites as vacancies provide strain relief to the deformed sample. NbC has also been found to pin grain boundaries during recrystallisation or allow for recrystallisation based on precipitate size. (Xiao, et al., 2012; Jones, et al., 1976; Mandal, et al., 2018).

## 3.2 Characterization of the as-cast structure

Figure 3 presents micrographs of the as-cast structure of the steel studied. The cast structure was found to have fine distribution of precipitates and inclusions within the chill zone of the slab. These were fine (average of 1.7 μm diameter through ImageJ analysis) due to the cooling rate at the chill zone favouring nucleation of particles as opposed to growth. Inclusions were found to be oxides such as Mg, Ca, Al and Si, whilst precipitates were found to be high in Fe, Cr, Nb and C. Due to the size of the particles, a definitive compositional analysis could not be provided through SEM-EDS.

The mid thickness of the cast consisted largely of columnar grains and the centre was defined by equiaxed grains. These precipitates were of crucifix form and measured to have an average leg length of 6.64 μm and 2.21 μm for the equiaxed and columnar regions respectively. Through SEM-EDS these were confirmed to be NbC precipitates.

Both the columnar and equiaxed zones, the precipitates were found to have nucleated and grown into a preferred orientation depending on the grain orientation. This was evidence that these precipitates formed after solidification as per the ThermoCalc predictions. Note that the crosses show the typical direction of precipitate orientation in adjacent grains while the arrows show precipitates observed at grain boundaries. These precipitates show that precipitates acted in grain boundary pinning, limiting grain growth (Jones, et al., 1976; Mandal, et al., 2018), Fig 3 (b) and (c). The finest precipitates were found in the chill zone, whilst precipitates in the equiaxed zone at the center of the slab were larger than in the columnar zone . This could be attributed to the high constitutional supercooling from the overlapping of the two solidification fronts.
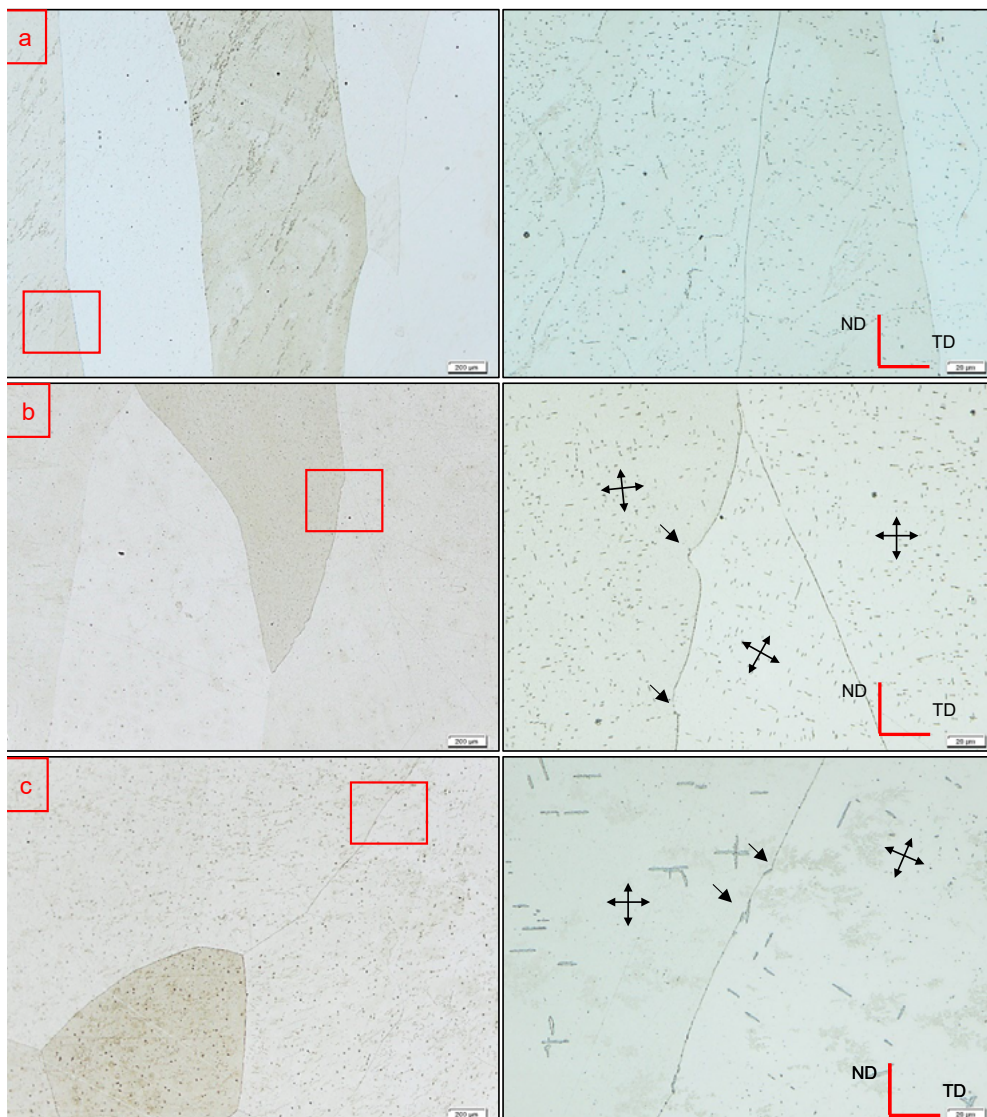
Figure 3: Micrographs of the cast structure showing grain characteristics a) around chill zone, b) columnar grain region and c) equiaxed region. The scale bars for micrographs on the left and right are 200 μm and 20 μm respectively.
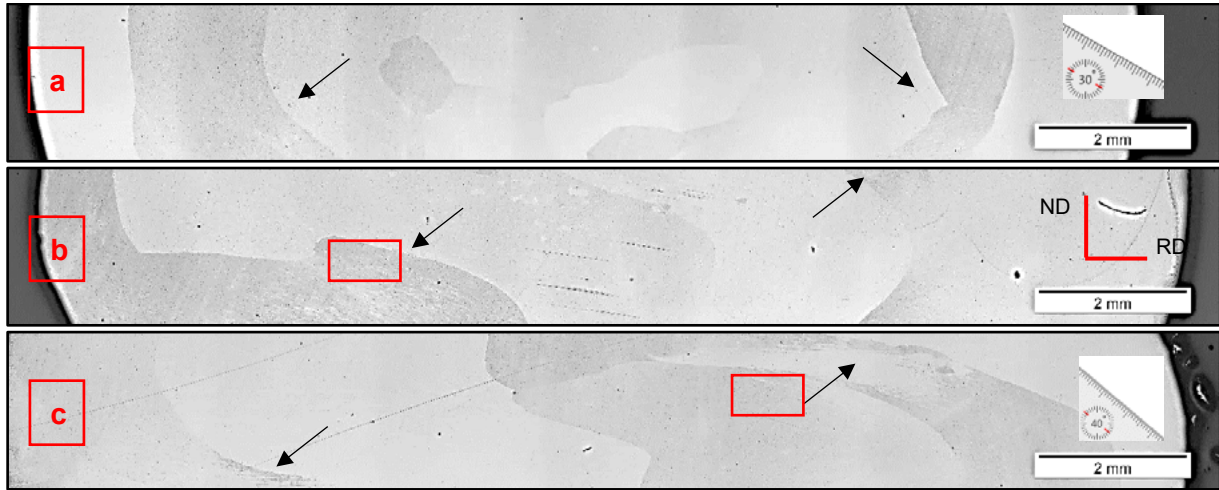
Figure 4: Microstructures of samples deformed under a) control b) increased inter-pass time (T1) and c) increased inter-pass time and increased strain (T2)

The increase in precipitate size towards the centre of the slab is typically expected due to the slower cooling rates allowing for more diffusion and subsequently, more time for orientated growth of precipitates, see Figure 3. (Xu, et al., 2011).

3.3 Thermomechanical simulations

3.3.1 Microstructural analysis

The two process routes, namely test T1 (increased inter-pass time only) and T2 (increased inter-pass time and strain), exhibited more grain curling, than the benchmark/control test, however, all three test conditions showed substantial shear bands, see arrows in Figure 4. These shear bands concentrated along the diagonal

corners of the deformed specimen and were aligned at 30 to 40° to the deformation axis. Included in the image are angle references for 30 and 40°.

Based on how samples deformed, the accumulation of strain was found at the centre and diagonals of the material during uniaxial testing, this is in line with work from Maubane where finite element modelling was used to define stress concentrations along deformed samples (Maubane, 2018). This would favour shear bands and subsequent recrystallisation as dislocations created would arrange into cellular structures forming stage 1 of the formation of new grains. Succeeding cycles of deformation would essentially lead to
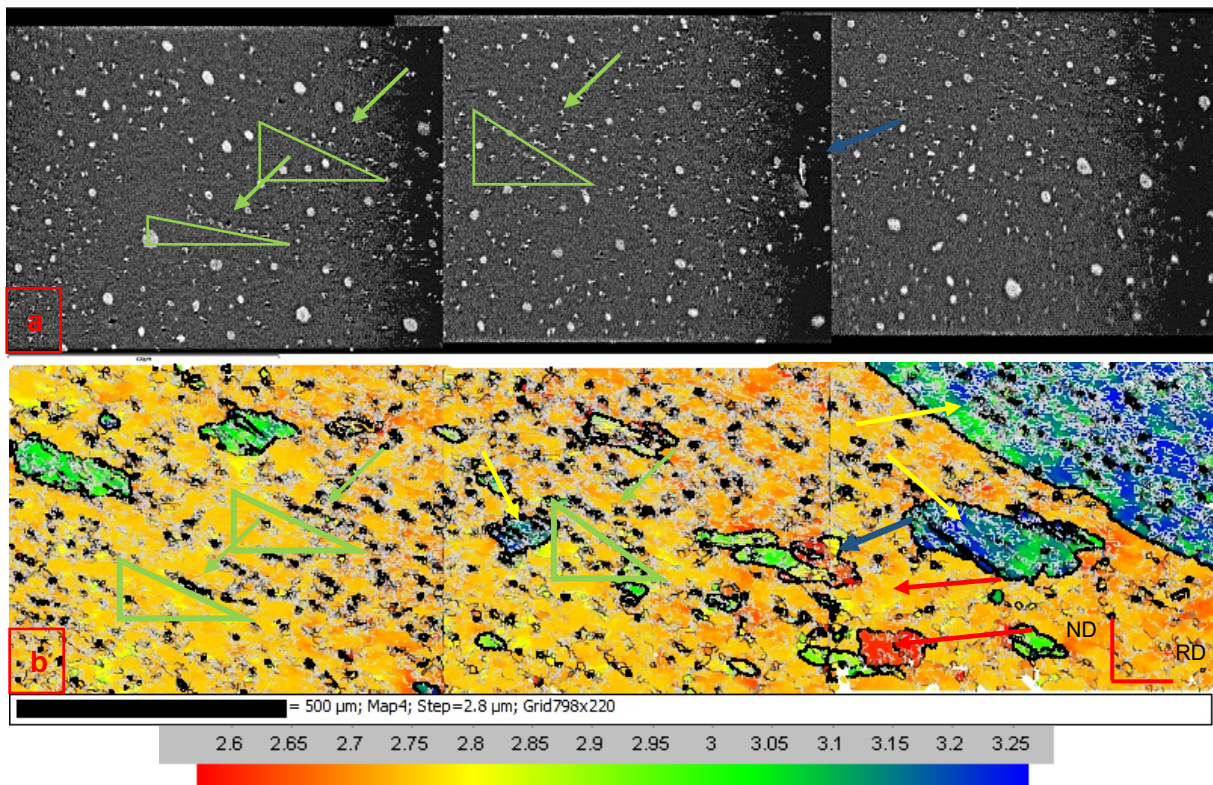
Figure 5: SEM micrographs of sample deformed at only increased inter-pass time showing a) array of precipitates that are aligned along the direction of shear bands b). High and low Taylor factor grains showing high and low angle grain boundaries
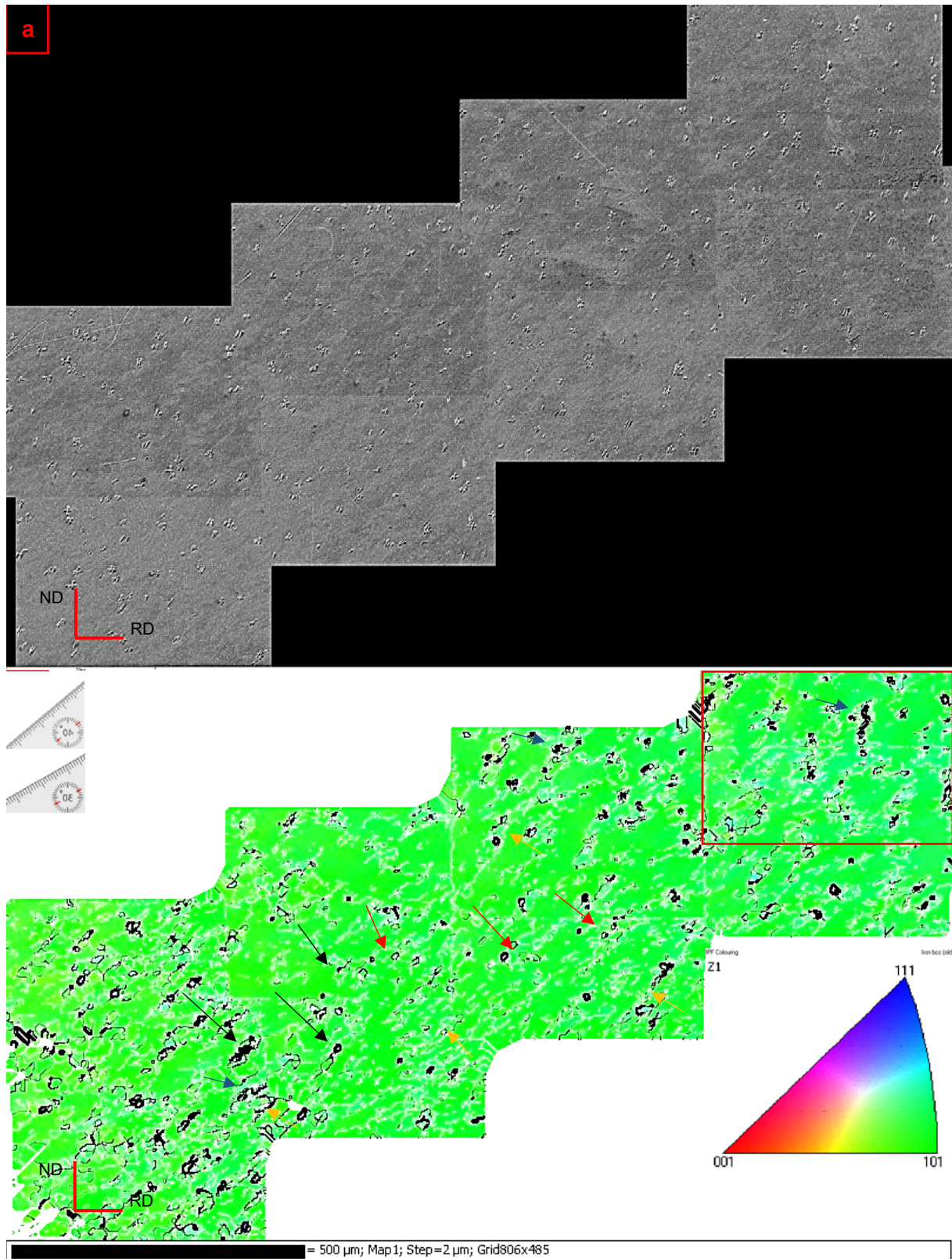
Figure 6: SEM images of samples deformed at an increased inter-pass time and increased strain showing a) distribution of precipitates and b) inverse pole figure indicating high and concentration of shear bands. Grain boundaries between 2-10° are depicted with silver and high angle boundaries in black.

an increase in grain misorientation and an increase in LAGB and HAGB concentration (Huang & Logé, 2016).

3.3.2 EBSD Analysis

Figure 5 shows SEM-EBSD images indicating a large array of precipitates that are aligned along the direction of shear bands

(arrowed in green). The EBSD image also shows Taylor factor representation of the microstructure with high Taylor factored grains (yellow arrow) being predominantly concentrated by low angle grain boundaries. Low Taylor factored grains (red and orange) show a relatively low concentration of low angle boundaries. Nucleation of grains around the inclusion, that had formed during
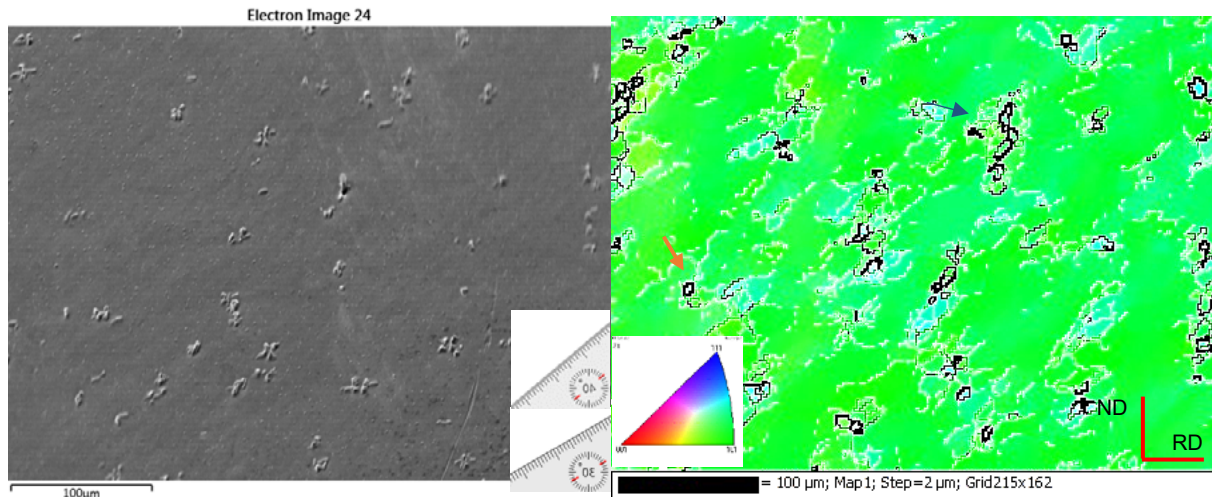
Figure 7: SEM and corresponding EBSD pole figure map for area enclosed in Figure 6. Arrowed in orange is a <111> grain.

casting (blue arrow in Figure 5) is visible through the presence of both high and low angle grain boundaries surrounding new grains. The EBSD image Figure 5(b) also shows the clear formation of shear bands within grains. These shear bands allow for grain recrystallisation along 30 and 45 degrees to the deformation direction. New grains forming are surrounded by both high and low angle grain boundaries that are aligned 30 to 45 degrees to the deformation directions. This shows that CDRX is occurring as these low angle grain boundaries are transforming into high angle grain boundaries with increased deformation. As these new grains are forming along 30 to 40 degree angles to the deformation direction they can be said to be driven by shear band formation.

Figure 6 presents a grains with <101>//ND of the sample deformed at an increased inter-pass time and increased strain (T2). Low angle grain boundaries are found to be orientated between 30 and 50° to the rolling direction (RD). Low angle grain boundaries are depicted in grey through the Channel 5 software. Some of the shear bands are highlighted by yellow arrows. The precipitates in Figure 6a, were found to be aligned with shear bands and were thus seen to have contributed to subsequent recrystallisation dynamics. This is seen more clearly in Figure 7.

The grain in Figure 6 also shows that recrystallised grains formed through CDRX were found to have specific orientations, in this case, CDRX grains had orientations going from the parent grain depicted in green (<101>//ND) to grains that are, turquois (<111>//ND) in colour. From research by Zhang, it was shown that recrystallisation from shear bands favours grains with <111>//ND orientations (Zhang, et al., 2011). The red arrows in Figure 6b show low angle boundaries (2-10°) that progressively result in the formation of high angle grain boundaries with accumulated strain (arrowed in black). This suggested the CDRX as a recovery mechanism and this is substantiated by the formation of low angle grain boundaries (grey in colour) around shear bands which subsequently evolved high angle grain boundaries (black in colour) with increased strain. Figure 7 gives an overview of the area enclosed in Figure 6. It offers a much clearer picture of what has been described.

In-grain shear bands or micro shear bands tend to be limited to the grain in which they occur, as apparent from EBSD imaging

presented in the study by (Mehtonen, 2014; Zhang, et al., 2011). The sub-grains and new grains formed displayed preferred new grain orientations as shown in Figure 6.

4.   Conclusion

In this study, the effects of inter-pass time and strain on the softening mechanism in 436 FSS were investigated. Based on the results and the analysis done, the following conclusions are drawn:

- PSN played a significant role as a recrystallization mechanism, with a high density of low angle grain boundaries surrounding precipitates.

- Both T1 and T2 samples showed a high concentration of low angle grain boundaries that are (depicted in grey) with less high angle grain boundaries (depicted in black). This indicates that a high stored deformation energy can be achieved with these methods which could translate to recrystallisation in subsequent hot rolling steps. Thus it can be said that an increase in interpass time and strain aids in increasing stored deformation energy.

5.   Acknowledgements

References

1. Thermo-Calc Software, 2019. *Thermo-Calc Version 2019b,* Solna: Thermo-Calc Software.
2. Annan, K. A., 2012. *Effect of Hot Working Characteristics on the Texture Development in AISI 430 and 433 Ferritic Stainless Steel,* Pretoria: University of Pretoria, Department of Materials Science and Metallurgical Engineering.
3. Annan, K. A., Siyasiya, C. W. & Stumpf, W., 2018. Austenite Grain Growth Kinetics after Isothermal deformation in Micro-alloyed Steels with varying Nb Concentrations. *Iron and Steel Institute of Japan,* Volume 58, pp. 333 - 339.
4. Braga, F. V., 2016. Hot deformation behavior of ferritic stainless steel stabilized with Nb during hot rolling simulation at different temperature ranges. *Journal of Materials Research,* 31(5), pp. 635-645.
5. Braga, F. V. et al., 2016. Recrystallization of niobium stabilized ferritic stainless steel during hot rolling simulation by torsion tests. *Journal of Materials Research and Technology,* 5(1), pp. 92-99.

6. Chao, H. C., 1971. Recent Studies into the Mechanism of Ridgin in Ferritic Stainless Steels. *Metallurgical Transactions,* Volume 4, pp. 1973-1183.

7. Columbus Stainless Steel Pty Ltd, 2020. *Downloads/Technical Brochures.* [Online] Available at: https://www.columbus.co.za/

8. Damstahl, 2015. Brochure. In: Damstahl, ed. *Technical Information.* Skanderborg: Damstahl, pp. 250-285.

9. Engler, O. & Randle, V., 2010. *Introduction to Texture Analysis: Macrotexture, Microtexture and Orientation.* 2 ed. New York: CRC Press.

10. Huang, K. & Logé, R., 2016. A review of dynamic recrystallization phenomena in metallic materials. *Journal of Materials and Design,* Volume 111, pp. 548-574.

11. Jones, A. R., Howell, P. R. & Ralph, B., 1976. The precipitation of niobium carbide at grain boundaries in an Austenitic Stainless Steel. *Journal of Materials Science,* Volume 11, pp. 1593-1599.

12. Lefebvre, G., 2014. *Relationship Between Microstructure, Texture and Ridging in Ferritic Stainless Steels,* Vancouver: University of British Columbia, Materials Engineering.

13. Maa, X. et al., 2019. Quantification of texture-induced ridging in ferritic stainless steels 430 and 430LR during tensile deformation. *Journal of Materials Research and Technology,* 8(2), pp. 2041-2051.

14. Mandal, G. K. et al., 2018. The role of precipitates in the recrystallisation mechanism of Nb-Mo micro-alloyed steel. *Journal of Materials Engineering and Performance,* Volume 27, pp. 6748-6757.

15. Maruma., M. G., 2013. *Effect of composition and thermomechanical processing on texture evolution, formability and ridging behaviour of ferritic stainless steel,* Pretoria: Department of Materials Science and Metallurgical Engineering, University of Pretoria.

16. Maubane, D. R. N., 2018. *The influence of roughing rolling conditions in peritectic microalloyed plate steels,* Pretoria: Department of Material Science and Metallurgical Engineering (University of Pretoria).

17. Mehtonen, S., 2014. *The behavior of stabilized high-chromium ferritic stainless steels in hot deformation,* Oulu: Acta Universitatis Ouluensis.

18. Mehtonen, S. et al., 2014. Microstructural and Texture Development during Multi-Pass Hot Deformation of a Stabilized High-Chromium Ferritic Stainless Steel. *ISIJ International,* 54(6), pp. 1406-1415.

19. Modak, P., Patra, S., Mitra, R. & Chakrabarti, D., 2018. Effect of Starting As-cast Structure on the Microstructure–Texture Evolution During Subsequent Processing and Finally Ridging Behavior of Ferritic Stainless Steel. *Metallurgical and Materials Transactions,* 49(A), pp. 2219-2234.

20. Siyasiya, C. W., 2007. *Effect of Sulphur content on the recrystallisation behaviour of cold-worked carbon Aluminiumkilled strip steels,* Pretoria: University of Pretoria.

21. Takechi, H., Kato, H., Sunami, T. & Nakayama, T., 1967. The Mechanism of Ridging Formation in 17% Chromium Stainless Steel Sheets. *Transactions of Japan Institute of Metals,* Volume 8, pp. 233-239.

22. Uananisa, H., Siyasiya, C. & Papo, W. S. a. M. J., 2016. The Influence of Thermomechanical Processing on the Surface Quality of an AISI 436 Ferritic Stainless Steel. *The Journal of The Southern African Institute of Mining and Metallurgy,* Volume 116, pp. 981-986.

23. Xiao, F. et al., 2012. Effect of Nb Solute and NbC Precipitates on Dynamic or Static recrystallisation of steel. *Journal of Iron and Steel Research, International,* 19(11), pp. 52-56.

24. Xu, K. et al., 2011. *Model of Microalloy Precipitation during Continuous Casting and Reheating.* Indianapolis, Association for Iron & Steel Technology.

25. Zhang, C., Liu, Z. & Wang, G., 2011. Effects of hot rolled shear bands on formability and surface ridging of an ultra-purified 21%Cr ferritic stainless steel. *Journal of Materials Processing Technology,* Volume 211, pp. 1051-1059.